Triaxial-band structures, chirality, and magnetic rotation in ^{133}La

C. M. Petrache,[1] Q. B. Chen,[2] S. Guo,[1,*] A. D. Ayangeakaa,[3,†] U. Garg,[3] J. T. Matta,[3,‡] B. K. Nayak,[3,§] D. Patel,[3,‖] J. Meng,[2] M. P. Carpenter,[4] C. J. Chiara,[4,5,¶] R. V. F. Janssens,[4] F. G. Kondev,[6] T. Lauritsen,[4] D. Seweryniak,[4] S. Zhu,[4] S. S. Ghugre,[7] and R. Palit[8,9]

[1]*Centre de Sciences Nucléaires et Sciences de la Matière, CNRS/IN2P3, and Université Paris-Saclay, Bât. 104-108, 91405 Orsay, France*
[2]*State Key Laboratory of Nuclear Physics and Technology, School of Physics, Peking University, Beijing 100871, China*
[3]*Department of Physics, University of Notre Dame, Notre Dame, Indiana 46556, USA*
[4]*Physics Division, Argonne National Laboratory, Argonne, Illinois 60439, USA*
[5]*Department of Chemistry and Biochemistry, University of Maryland, College Park, Maryland 20742, USA*
[6]*Nuclear Engineering Division, Argonne National Laboratory, Argonne, Illinois 60439, USA*
[7]*UGC-DAE Consortium for Science Research, Kolkata 700 098, India*
[8]*Tata Institute of Fundamental Research, Mumbai 400 005, India*
[9]*Joint Institute for Nuclear Astrophysics, University of Notre Dame, Notre Dame, Indiana 46556, USA*

(Received 17 May 2016; revised manuscript received 29 August 2016; published 5 December 2016)

The structure of ^{133}La has been investigated using the ^{116}Cd(^{22}Ne ,4pn) reaction and the Gammasphere array. Three new bands of quadrupole transitions and one band of dipole transitions are identified and the previously reported level scheme is revised and extended to higher spins. The observed structures are discussed using the cranked Nilsson-Strutinsky formalism, covariant density functional theory, and the particle-rotor model. Triaxial configurations are assigned to all observed bands. For the high-spin bands it is found that rotations around different axes can occur, depending on the configuration. The orientation of the angular momenta of the core and of the active particles is investigated, suggesting chiral rotation for two nearly degenerate dipole bands and magnetic rotation for one dipole band. It is shown that the $h_{11/2}$ neutron holes present in the configuration of the nearly degenerate dipole bands have significant angular momentum components not only along the long axis but also along the short axis, contributing to the balance of the angular momentum components along the short and long axes and thus giving rise to a chiral geometry.

DOI: 10.1103/PhysRevC.94.064309

I. INTRODUCTION

The recent discovery of the transverse wobbling mode in the odd-even ^{135}Pr nucleus [1], where collectively enhanced $\Delta I = 1$ transitions with $E2$ character between the one- and zero-phonon rotational bands were observed, along with with a decreasing wobbling frequency, is currently attracting a great deal of attention. The manifestation of this mode signals the stability of triaxial deformation in nuclei of the $A \approx 130$ mass region. In addition to nuclear wobbling, the chiral mode provides another key fingerprint of triaxiality which manifests itself when the rotation axis is tilted with respect to the principal axes of the triaxially deformed density distribution [2]. Investigations of these two modes of collective-triaxial rotation encompass a great majority of experimental efforts in this mass region.

The most recent studies of the La nuclei of this mass region have been driven mainly by the search for chiral partner bands. Experimentally, candidates for chiral partners have been observed in the odd-odd ^{130}La [3], ^{132}La [4], and ^{134}La [5] isotopes. The study of odd-even La nuclei provides another dimension to these investigations, especially in light of the observation of multiple chiral-doublet (MχD) bands in the odd-A ^{133}Ce nucleus [6] and the aforementioned case of transverse wobbling in ^{135}Pr [1]. In addition, the odd-A cases are important to verifying indications of substantially reduced pairing in multiquasiparticle configurations associated with chiral bands and provide an important confirmation of the geometrical interpretation of chiral rotation.

In this paper, we report on new experimental results on the odd-A ^{133}La nucleus obtained from a high-statistics experiment performed at the ATLAS accelerator facility with the Gammasphere array. Three new bands of quadrupole transitions and one band of dipole γ rays were identified at high spins. In addition, many of the previously reported transitions have been placed differently in the level scheme. Two previously known dipole bands are confirmed and improved upon with connecting transitions at high spins. The anisotropy and the angular-distribution coefficients of many transitions are determined. The observed bands are discussed in the framework of the cranked Nilsson-Strutinsky (CNS) model as described in Refs. [7–10], the covariant

[*]On leave from Institute of Modern Physics, Chinese Academy of Sciences, Lanzhou 730000, China.
[†]Present address: Physics Division, Argonne National Laboratory, Argonne, Illinois 60439, USA.
[‡]Present address: Physics Division, Oak Ridge National Laboratory, Oak Ridge, Tennessee 37830, USA.
[§]Present address: Nuclear Physics Division, Bhabha Atomic Research Centre, Mumbai 400 085, India.
[‖]Present address: M.D. Anderson Cancer Center, Houston, Texas 77030, USA.
[¶]Present address: U.S. Army Research Laboratory, Adelphi, Maryland 20783, USA.

energy density functional theory (CDFT) with self-consistent relativistic mean field (RMF) [11], and the particle-rotor model (PRM) [6,12–15]. Triaxial configurations are assigned to all observed bands. The analysis of the collective and single-particle angular momenta components along the three axes of the intrinsic reference frame suggests chiral rotation for two nearly degenerate dipole bands and magnetic rotation for one dipole band.

II. EXPERIMENTAL DETAILS

The present work is the fourth in a series of papers reporting results from the same measurement. Hence, the experimental procedure and the analysis methods are similar and only briefly summarized here. The reader is referred to Refs. [6,16] for further details. The experiment was performed at the ATLAS superconducting linear accelerator facility at Argonne National Laboratory (ANL) where the ^{133}La nucleus was populated in two separate experiments following the ^{116}Cd(^{22}Ne , $p4n$) reaction. In the first one, a 112-MeV beam of ^{22}Ne bombarded a 1.48-mg/cm^2-thick foil of isotopically enriched ^{116}Cd, sandwiched between a 50-μg/cm^2-thick front layer of Al and a 150-μg/cm^2 Au backing. The second experiment used the same beam and a target of the same enrichment and thickness but evaporated onto a 55-μg/cm^2-thick Au foil. The Gammasphere array [17], which comprised 101 (88) active Compton-suppressed HPGe detectors during the first (second) experiment, was used to detect the γ rays emitted by the residual nuclei. The accumulated data were unfolded and sorted into fully symmetrized, three-dimensional (E_γ-E_γ-E_γ) and four-dimensional (E_γ-E_γ-E_γ-E_γ) histograms of γ-ray energies, E_γ, and analyzed using the RADWARE analysis package [18,19]. Transition multipolarity assignments were made on the basis of angular-distribution measurements [20] and, for weak transitions, on a two-point angular-correlation ratio, R_{ac} [21,22]. The energies, relative intensities, and associated angular-distribution coefficients and R_{ac} ratios as well as the multipolarity assignments for the observed transitions are presented in Table I.

III. RESULTS AND LEVEL SCHEME

A partial ^{133}La level scheme displaying the low- and medium-spin states observed in the present investigation is presented in Fig. 1. The newly identified high-spin bands $Q8$, $Q9$, and $Q10$, and the corresponding double-gated spectra, can be found in Figs. 2 and 3, respectively. In the following, only those parts of the observed bands for which new transitions have been observed, or for which a new interpretation is proposed, are discussed.

Band $D1$, which was first reported in Ref. [23], is confirmed in this study with the addition of five new transitions of 431, 446, 876, 877, and 931 keV on top of the structure reported previously. The ratios of reduced transition probabilities extracted from the present data set are provided in Fig. 4.

The band labeled $D4$ in Fig. 1 is composed of 11 states connected by dipole transitions. It decays directly and indirectly to the negative-parity yrast band $Q1$. Some of the in-band transitions were reported previously, but placed differently. The present high-statistics data set allowed the disentanglement of the 445.7-448.1-448.3-keV triplet and of the 348.4-350.1-keV doublet. The ordering of the in-band transitions was further facilitated by the new 923-keV crossover transition, the parallel 446-479-keV cascade and the 944-keV link to the $35/2^-$ state of band $Q1$, and is now firmly established. The bandhead spin-parity $27/2^-$ was fixed previously by the angular distribution results of Ref. [23]. From the present experiment it was possible to measure the $B(M1)/B(E2)$ branching ratio of 10.14(15) for the $35/2^-$ state, which is depopulated by the 475-keV dipole and the 923-keV crossover transitions. The nonobservation of the other crossover transitions in band $D4$ implies that the branching ratios are much higher than 10; this could be indicative of magnetic rotation.

Band $Q8$ (see Fig. 2) is the continuation at higher spins of the negative-signature partner ($\alpha = -1/2$) of band $D1$. We note here that the signature is defined when the rotation is around a principal axis of the intrinsic coordinate system, which is the case in the framework of the CNS model, but not when the rotation is around a tilted axis, like in the case of the PRM model. In the following we will use the terms *signature partners* or *signature splitting* even outside the CNS framework when discussing the different bands, keeping in mind that for rotation around a tilted axis the two signatures are mixed. Band $Q8$ is composed of six newly identified states connected by weak transitions for which an $E2$ character is assumed. Similarly, an $E2$ character is assumed for transitions in band $Q9$ which is composed of eight levels. The decay transitions from band $Q9$ to low-lying states could not be identified, but from the analysis of coincidence transitions, it was concluded that the main decay paths are towards the bands $D1$, $D2$, $Q1$ and $D4$. The spin parity of the band is proposed based on comparisons with the CNS calculations (see below).

A similar situation exists for the high-spin band labeled $Q10$ in Fig. 2, composed of 10 states: The connecting transitions are assumed to have $E2$ character; the decay transitions towards low-lying states could not be identified, but it was concluded that the main decay paths are towards band $Q1$ and $D4$ based on the observed coincidence transitions, and the spin parity of the band is based on comparisons with CNS calculations (see below).

IV. DISCUSSION

In this section, spectroscopic properties of the newly observed bands in ^{133}La are investigated in detail by comparison with neighboring nuclei to find the most probable configurations. These are checked further with the help of the cranked Nilsson-Strutinsky (CNS) model, the covariant density functional theory (CDFT) with a self-consistent relativistic mean field (RMF), and the particle rotor model (PRM) [6,12–15]. The deformation parameters for the assigned configurations obtained from the CNS calculations are compared with those of the CDFT calculations to check the consistency of the adopted deformation parameter sets used as input for the PRM calculations. The deformation parameters from the CDFT calculations were obtained by performing both the adiabatic and configuration-fixed constrained calculations [11]. Due to

TABLE I. Energies of γ rays E_γ and initial levels E_i, angular-distribution coefficients A_2 and A_4, angular-correlation ratios R_{ac}, multipolarities, and spin-parity assignments of the initial and final levels for γ-ray transitions in ^{133}La.

E_γ^a (keV)	E_i (keV)	A_2	A_4	R_{ac}	Multipolarity	$J_i^\pi \rightarrow J_f^\pi$
Band $Q8$						
960.3	7242.1					$(43/2^+)\rightarrow(39/2^+)$
980.6	8222.7	0.32(3)	0.00(4)	1.30(10)	$E2$	$(47/2^+)\rightarrow(43/2^+)$
1024.3	9247.0					$(51/2^+)\rightarrow(47/2^+)$
1117.7	10364.7					$(55/2^+)\rightarrow(51/2^+)$
1219.1	11583.8					$(59/2^+)\rightarrow(55/2^+)$
1325.8	12909.6					$(63/2^+)\rightarrow(59/2^+)$
Band $Q9$						
870.7						$(45/2^+)\rightarrow(41/2^+)$
962.9						$(49/2^+)\rightarrow(45/2^+)$
1046.2						$(53/2^+)\rightarrow(49/2^+)$
1143.0		0.52(11)	0.20(14)	1.41(16)	$E2$	$(57/2^+)\rightarrow(53/2^+)$
1231.9						$(61/2^+)\rightarrow(57/2^+)$
1342.8						$(65/2^+)\rightarrow(61/2^+)$
1402.8						$(69/2^+)\rightarrow(65/2^+)$
Band $Q10$						
796.7						$(45/2^-)\rightarrow(41/2^-)$
931.3						$(49/2^-)\rightarrow(45/2^-)$
1040.1						$(53/2^-)\rightarrow(49/2^-)$
1137.7						$(57/2^-)\rightarrow(53/2^-)$
1252.5						$(61/2^-)\rightarrow(57/2^-)$
1364.5						$(65/2^-)\rightarrow(61/2^-)$
1481.7						$(69/2^-)\rightarrow(65/2^-)$
1591.1						$(73/2^-)\rightarrow(69/2^-)$
1694.4						$(77/2^-)\rightarrow(73/2^-)$
Band $D1$						
77.3	2367.4					$17/2^+\rightarrow(15/2^+)$
135.2	2502.6	$-0.17(3)$	0.02(4)	0.86(5)	$M1/E2$	$19/2^+\rightarrow17/2^+$
146.9	2367.4					$17/2^+\rightarrow(13/2^+)$
178.8	2681.4	$-0.22(2)$	0.08(3)	0.82(5)	$M1/E2$	$21/2^+\rightarrow19/2^+$
212.5	2502.6					$19/2^-\rightarrow(15/2^+)$
245.7	2927.1	$-0.40(1)$	0.12(1)	0.71(4)	$M1/E2$	$23/2^+\rightarrow21/2^+$
314.0	2681.4					$21/2^+\rightarrow17/2^+$
330.8	3257.9	$-0.53(1)$	0.02(2)	0.65(4)	$M1/E2$	$25/2^+\rightarrow23/2^+$
355.9	3613.8	$-0.49(2)$	0.00(3)	0.89(4)	$M1/E2$	$27/2^+\rightarrow25/2^+$
415.7	4029.5	$-0.67(3)$	0.06(4)	0.58(4)	$M1/E2$	$29/2^+\rightarrow27/2^+$
424.5	2927.1					$23/2^+\rightarrow19/2^+$
431.3	4905.4	$-0.63(6)$	0.06(7)	0.61(4)	$M1/E2$	$33/2^+\rightarrow31/2^+$
444.6	4474.1	$-0.47(4)$	0.00(6)	0.71(5)	$M1/E2$	$31/2^+\rightarrow29/2^+$
445.9	5351.3					$(35/2^+)\rightarrow33/2^+$
576.5	3257.9					$25/2^+\rightarrow21/2^+$
686.7	3613.8					$27/2^+\rightarrow23/2^+$
771.6	4029.5	0.54(8)	$-0.17(11)$	1.52(13)	$E2$	$29/2^+\rightarrow25/2^+$
860.3	4474.1					$31/2^+\rightarrow27/2^+$
875.9	4905.4	0.25(9)	0.00(12)	1.12(8)	$E2$	$33/2^+\rightarrow29/2^+$
877.2	5351.3					$(35/2^+)\rightarrow31/2^+$
930.5	6281.8	0.49(6)	$-0.11(8)$	1.45(13)	$E2$	$(39/2^+)\rightarrow(35/2^+)$
231.9	3613.8	0.35(3)	$-0.05(4)$	1.30(10)	$M1/E2$	$27/2^+\rightarrow25/2^+$
336.2	3613.8	$-0.44(2)$	0.02(3)	0.71(4)	$M1/E2$	$27/2^+\rightarrow25/2^+$
367.5	3257.9	$-0.50(1)$	$-0.01(2)$	0.68(5)	$M1/E2$	$25/2^+\rightarrow23/2^+$
414.0	2367.4					$17/2^+\rightarrow15/2^+$
419.1	2681.4					$21/2^+\rightarrow19/2^+$
427.4	2502.6					$19/2^+\rightarrow17/2^+$
462.8	4474.1					$31/2^+\rightarrow(29/2^+)$
552.1	2367.4					$17/2^+\rightarrow(15/2^+)$
843.2	2220.5					$(13/2^+)\rightarrow15/2^+$

TABLE I. *(Continued.)*

E_γ^a (keV)	E_i (keV)	A_2	A_4	R_{ac}	Multipolarity	$J_i^\pi \rightarrow J_f^\pi$
990.1	2367.4	−0.29(4)	0.03(5)	0.76(5)	$M1/E2$	$17/2^+ \rightarrow 15/2^+$
1101.7	2290.1					$(15/2^+) \rightarrow 13/2^+$
1106.7	2367.4					$17/2^+ \rightarrow 13/2^+$
1125.3	2502.6					$19/2^+ \rightarrow 15/2^+$
1179.0	2367.4	0.30(4)	−0.02(5)	1.23(8)	$E2$	$17/2^+ \rightarrow 13/2^+$
Band $D2$						
167.1	2893.2					$21/2^+ \rightarrow 19/2^+$
217.1	3110.3	−0.39(11)	0.12(15)	0.75(9)	$M1/E2$	$23/2^+ \rightarrow 21/2^+$
271.6	3381.9	−0.60(3)	−0.13(3)	0.65(5)	$M1/E2$	$25/2^+ \rightarrow 23/2^+$
355.9	4133.5					$29/2^+ \rightarrow 27/2^+$
384.2	3110.3					$23/2^+ \rightarrow 19/2^+$
395.7	3777.6					$27/2^+ \rightarrow 25/2^+$
488.7	3381.9					$25/2^+ \rightarrow 21/2^+$
667.3	3777.6					$27/2^+ \rightarrow 23/2^+$
751.6	4133.5					$29/2^+ \rightarrow 25/2^+$
390.6	2893.2					$21/2^+ \rightarrow 19/2^+$
428.9	3110.3					$23/2^+ \rightarrow 21/2^+$
454.8	3381.9					$25/2^+ \rightarrow 23/2^+$
519.7	3777.6					$27/2^+ \rightarrow 25/2^+$
519.7	4133.5					$29/2^+ \rightarrow 27/2^+$
607.7	3110.3					$23/2^+ \rightarrow 19/2^+$
700.5	3381.9					$25/2^+ \rightarrow 21/2^+$
854.3	2893.2					$21/2^+ \rightarrow 17/2^+$
Band $D3$						
365.0	4011.3					$29/2^+ \rightarrow 27/2^+$
416.0	4925.8					$33/2^+ \rightarrow 31/2^+$
498.5	4509.8					$31/2^+ \rightarrow 29/2^+$
542.5	3646.3					$27/2^+ \rightarrow 25/2^+$
863.5	4509.8					$31/2^+ \rightarrow 27/2^+$
907.5	4011.3	0.37(5)	−0.13(7)	1.42(10)	$E2$	$29/2^+ \rightarrow 25/2^+$
914.5	4925.8	0.22(8)	−0.27(11)	1.27(10)	$E2$	$33/2^+ \rightarrow 29/2^+$
213.4	3103.8	−0.32(2)	0.09(2)	0.75(5)	$M1/E2$	$25/2^+ \rightarrow 23/2^+$
Band $D4$						
348.4	3947.8	−0.51(2)	0.08(3)	0.65(4)	$M1/E2$	$29/2^- \rightarrow 27/2^-$
350.1	7027.5					$(43/2^-) \rightarrow (41/2^-)$
389.3	6141.7	−0.55(4)	−0.01(5)	0.65(4)	$M1/E2$	$39/2^- \rightarrow 37/2^-$
433.7	5752.4	−0.62(2)	0.13(3)	0.48(4)	$M1/E2$	$37/2^- \rightarrow 35/2^-$
445.7	6198.1					$(39/2^-) \rightarrow 37/2^-$
448.1	4844.2					$33/2^- \rightarrow 31/2^-$
448.3	4396.1	−0.53(1)	0.08(2)	0.64(4)	$M1/E2$	$31/2^- \rightarrow 29/2^-$
474.5	5318.7	−0.34(3)	0.02(4)	0.76(4)		$35/2^- \rightarrow 33/2^-$
479.3	6677.4					$(41/2^-) \rightarrow (39/2^-)$
535.7	6677.4					$(41/2^-) \rightarrow 39/2^-$
584.3	7611.8					$(45/2^-) \rightarrow (43/2^-)$
922.6	5318.7	0.26(4)	−0.03(6)	1.20(8)	$E2$	$35/2^- \rightarrow 31/2^-$
151.4	3599.4	−0.26(3)	−0.03(4)	0.82(5)	$M1/E2$	$27/2^- \rightarrow 25/2^-$
168.5	3599.4	−0.32(5)	0.15(7)	0.71(5)	$M1/E2$	$27/2^- \rightarrow 25/2^-$
307.3	3599.4	0.31(5)	0.21(7)	1.22(9)	$M1/E2$ ($\Delta I = 0$)	$27/2^- \rightarrow 27/2^-$
595.0	3599.4					$27/2^- \rightarrow (23/2^-)$
913.5	3448.0	0.35(3)	−0.05(4)	1.30(10)	$E2$	$25/2^- \rightarrow 21/2^-$
944.3	6141.7					$39/2^- \rightarrow 35/2^-$
998.2	3448.0	−1.29(17)	0.51(20)	0.25(3)	$M1/E2$	$25/2^- \rightarrow 23/2^-$
1149.6	3599.4					$27/2^- \rightarrow 23/2^-$
Other states						
209.0	2890.4	−0.26(1)	0.10(2)	0.80(5)	$M1/E2$	$23/2^+ \rightarrow 21/2^+$
350.5	3277.6	−0.57(4)	0.00(5)	0.66(4)	$M1/E2$	$25/2^+ \rightarrow 23/2^+$
387.2	3277.6	−0.55(2)	0.04(2)	0.63(4)	$M1/E2$	$25/2^+ \rightarrow 23/2^+$

TABLE I. (*Continued.*)

E_γ^a (keV)	E_i (keV)	A_2	A_4	R_{ac}	Multipolarity	$J_i^\pi \rightarrow J_f^\pi$
440.4	4054.2					$(29/2^+) \rightarrow 27/2^+$
462.8	4936.9					$(33/2^+) \rightarrow 31/2^+$
491.8	5428.7	−1.29(17)	0.51(20)	0.25(3)	$M1/E2$	$(35/2^+) \rightarrow (33/2^+)$
776.6	4054.2					$(29/2^+) \rightarrow 25/2^+$

limitations in the valence space of the PRM, configuration assignments for the high-spin bands were achieved using the CNS calculations only.

A. Quasiparticle alignment analysis

The results of the quasiparticle alignment analysis [24] of the observed bands $Q1$, $Q2$, $Q8$, $Q9$, $Q10$, $D1$, $D2$, and $D4$ in ^{133}La are presented in Fig. 5. The Harris parameters used to extract the quasiparticle alignments are $\mathcal{J}_0 = 10\hbar^2/\text{MeV}$ and $\mathcal{J}_1 = 20\hbar^4/\text{MeV}^3$; $K = 0$ has been adopted for the projection of the total angular momentum on the z axis.

The alignments of bands $Q1$ and $Q2$ are similar—$\sim 7\hbar$ for $\hbar\omega \sim 0.3$–0.4MeV, gradually increasing up to the highest observed spins. Considering the similarity between the bands and the lowest-lying negative-parity bands in other odd-even neighboring nuclei (e.g., ^{135}Pr [1]), the $\pi(h_{11/2})^1$ configuration is assigned to these bands.

The alignments of bands $D1$ and $D2$ are almost the same, 9–$10\hbar$, and are higher than those of bands $Q1$ and $Q2$ by $\sim 3\hbar$. The higher alignments and excitation energies of these bands can be explained only by invoking three-quasiparticle configurations. The configuration assigned in Ref. [23] is $\pi(d_{5/2},g_{7/2})^1 \otimes \nu(h_{11/2})^{-2}$. However, the $\pi(h_{11/2})^1 \otimes \nu(s_{1/2},d_{3/2})^{-1}(h_{11/2})^{-1}$ alternative configuration can also account for the properties of bands $D1$ and $D2$, excepting their decay, which is observed only towards the bands Q_1–Q_4 based on the $\pi(d_{5/2},g_{7/2})$ orbitals. The observed decay pattern strongly suggests a similar $\pi(d_{5/2},g_{7/2})$ proton configuration for the bands $D1$, $D2$, and Q_1–Q_4, which induces us to adopt the $\pi(d_{5/2},g_{7/2})^1 \otimes \nu(h_{11/2})^{-2}$ configuration previously assigned in Ref. [23] to the bands $D1$ and $D2$.

As stated previously, band $Q8$ is the continuation at high spin of the negative-signature partner of band $D1$. As can be seen in Fig. 5, the alignment of band $Q8$ increases to $\sim 20\hbar$ at the highest observed spins, a value higher than that of band $D1$ by $\sim 10\hbar$. This observation clearly indicates the presence of two additional $\pi h_{11/2}$ protons aligned along the rotation axis. Therefore, the $\pi(d_{5/2},g_{7/2})^1(h_{11/2})^2 \otimes \nu(h_{11/2})^{-2}$ configuration is assigned to band $Q8$.

The alignment of band $D4$ is $\sim 11\hbar$ for $\hbar\omega \leqslant 0.45$ MeV, being higher by $\sim 1.5\hbar$ than that of the bands $D1$ and $D2$.

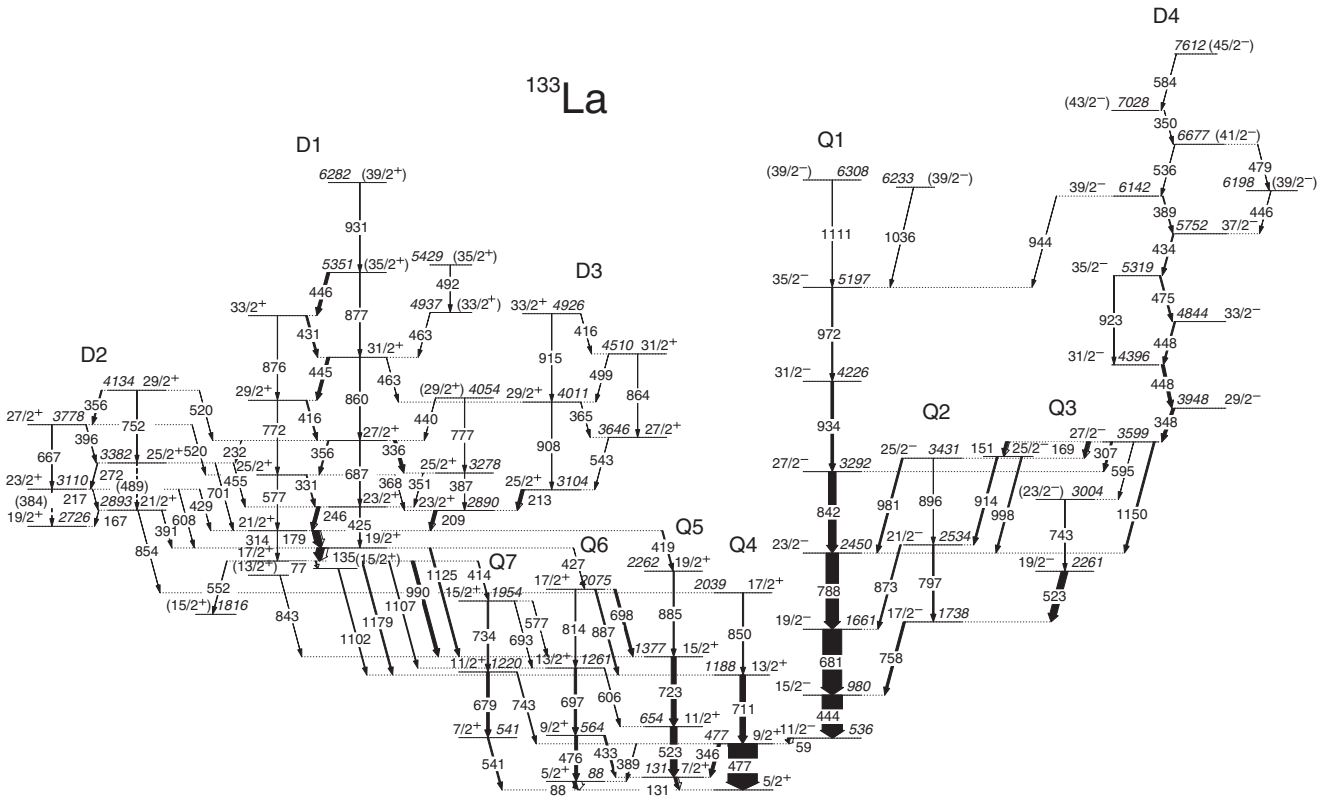

FIG. 1. Partial level scheme of ^{133}La showing the low- and medium-spin states. Arrow widths are proportional to γ-ray intensities.

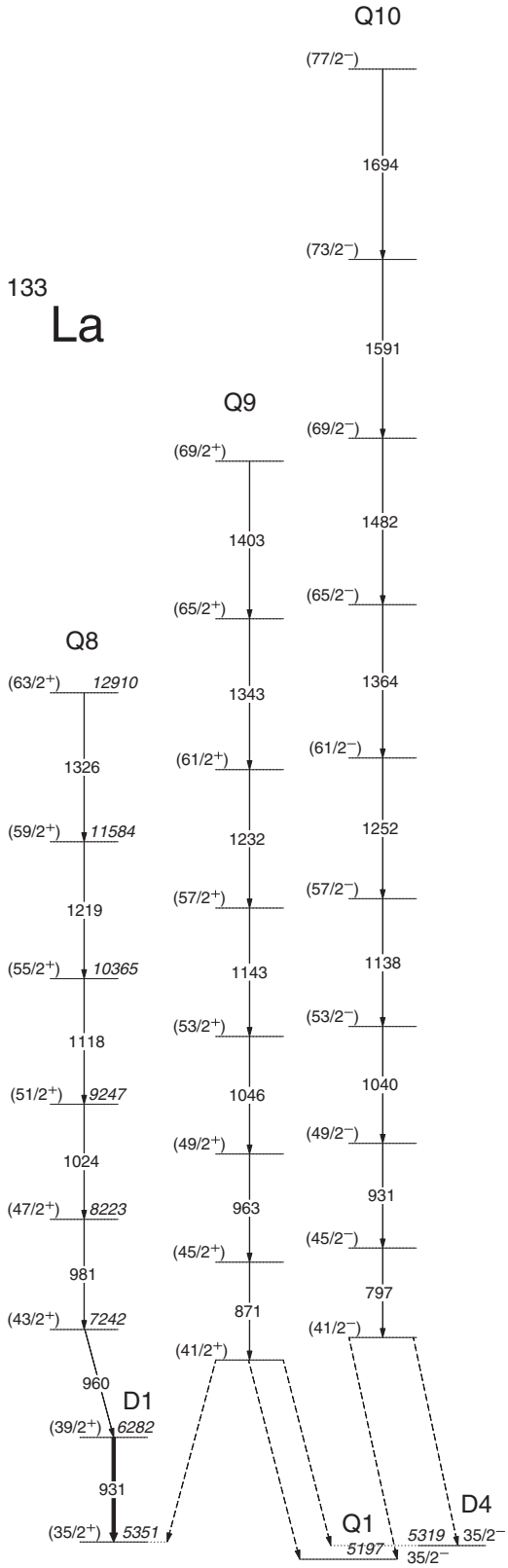

FIG. 2. Partial level scheme of ^{133}La with the high-spin bands (see text for details).

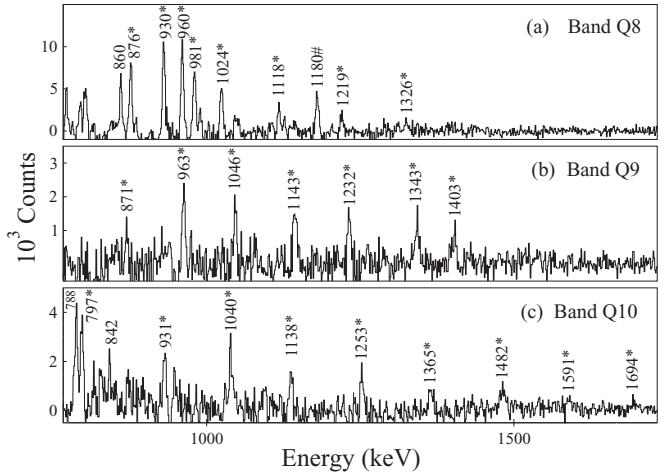

FIG. 3. Double-gated coincidence spectra for the newly identified bands $Q8$, $Q9$, and $Q10$ of ^{133}La. The spectrum of band $Q8$ is obtained by summing the spectra with a gate on the 135-, 179-, 209- and 331-keV transitions of band $D1$ and a second gate on the in-band transitions. The spectrum of band $Q9$ is obtained by summing the spectra double-gated on all combinations of the in-band transitions (except 963 and 871 keV), and the 179-keV γ ray of band $D1$. The spectrum of band $Q10$ is obtained by summing the spectra double-gated on combinations of all in-band transitions (except 1591 and 1694 keV). Transitions marked with asterisks represent the band members, while those marked with # are identified contaminants from other bands.

The band is composed of strong dipole transitions and weak crossover quadrupole transitions, which is characteristic of tilted axis rotation. It is tempting to assign the $\pi(h_{11/2})^1 \otimes \nu(h_{11/2})^{-2}$ configuration to band $D4$, which represents a simple excitation of one proton from the $\pi(d_{5/2},g_{7/2})$ orbital to the $\pi h_{11/2}$ state relative to the configuration of bands $D1$ and $D2$. The Pythagorean sum of the orthogonal angular momenta of the active particles gives $11.4\hbar$, which is close to the $\sim 11\hbar$

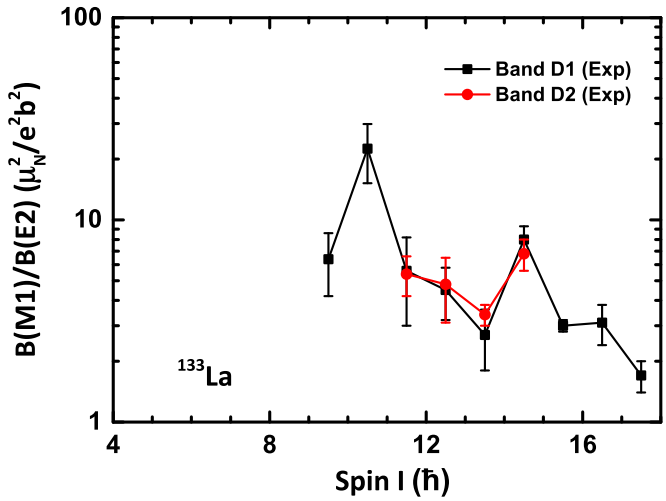

FIG. 4. The $B(M1)/B(E2)$ ratios of bands $D1$ and $D2$ of ^{133}La. The solid lines linking the experimental values are meant to guide the eye.

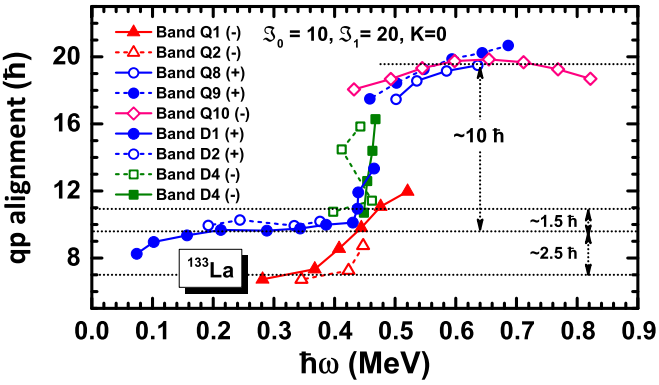

FIG. 5. Quasiparticle alignment as a function of rotational frequency for bands $Q1$, $Q2$, $Q8$, $Q9$, $Q10$, $D1$, $D2$, and $D4$ in ^{133}La. The Harris parameters used are $\mathcal{J}_0 = 10\hbar^2/\text{MeV}$ and $\mathcal{J}_1 = 20\hbar^4/\text{MeV}^3$, and the projection of the total angular momentum on the z axis is $K = 0$ in all cases. The parity of the bands is also indicated in the legend. For band $D4$, the solid line with full symbols denotes the $\alpha = +1/2$ sequences, while the dashed line with empty symbols denotes the $\alpha = -1/2$ sequences.

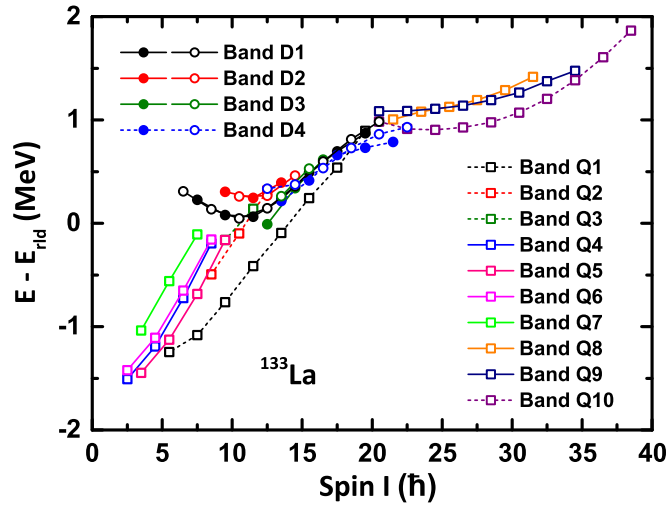

FIG. 6. Energies relative to a standard rotating liquid drop reference calculated for the experimental bands observed in ^{133}La. The labeling of the configurations is explained in the text. With an odd number of $h_{11/2}$ neutron holes, two signature-degenerate bands are formed, which are shown by the same color and symbols. For the dipole bands, the closed symbols denote the $\alpha = +1/2$ sequences, while the open symbols denote the $\alpha = -1/2$ sequences.

experimental value. At $\hbar\omega \sim 0.45$ MeV, a sudden increase of the alignment is observed, indicating a crossing with a five-quasiparticle configuration, and the $\pi(h_{11/2})^3 \otimes \nu(h_{11/2})^{-2}$ configuration may plausibly be assigned to the higher part of band $D4$. However, one should note that the behavior of band $D4$ is quite irregular, with the two signature partners having different patterns. The present formalism does not allow detailed insight into the band structure and the mechanism involved in the configuration change in the crossing region, which occurs at a frequency similar to that of the bands $D1$ and $D2$, even if the alignment of a $h_{11/2}$ proton pair should be blocked. This question remains unexplained.

The alignments of the bands $Q9$ and $Q10$, resulting from the assumed spins and energies of the bands, increase over the observed frequency range to $\sim 20\hbar$. As the alignment of band $Q9$ follows closely that of band $Q8$, most probably the same orbitals are involved in both bands. Based also on CNS calculations (see Subsec. IV B), we assign a $\pi(d_{5/2},g_{7/2})^1 h_{11/2}^2 \otimes \nu h_{11/2}^{-2}$ configuration to band $Q9$, similar to that assigned to band $Q8$, and a $\pi(d_{5/2},g_{7/2})^1 h_{11/2}^2 \otimes \nu(s_{1/2},d_{3/2})^{-1} h_{11/2}^{-2}(h_{9/2},f_{7/2})^1$ configuration to band $Q10$.

B. CNS calculations

The level structure of ^{133}La, with 57 protons and 76 neutrons, can be considered to arise mainly from the interaction between seven proton valence particles out of the $Z = 50$ major shell and six neutron holes in the $N = 82$ major shell. However, highly excited or very deformed configurations can also involve breaking of the $Z = 50$ core or excitations above the $N = 82$ shell closure. In the low-energy regime, the nucleus is expected to have a small deformation, $\varepsilon_2 \sim 0.15$–0.20. It is convenient, therefore, to express the single-particle states in terms of j-shell quantum numbers.

In the CNS formalism, the nucleus rotates about one of its principal axes and pairing is neglected. The deformation is optimized for each configuration explored. The configurations are labeled by the number of particles in low-j and high-j orbitals, in the different $\mathcal{N}$ shells. They can be defined relative to a ^{132}Sn core as

$$\pi(dg)^{p_1}(h_{11/2})^{p_2}\nu(sd)^{-n_1}(h_{11/2})^{-n_2}(hf)^{n_3}(i_{13/2})^{n_4},$$

for which the short-hand notation $[p_1p_2,n_1n_2(n_3n_4)]$ is used. The pseudospin partners $d_{5/2}g_{7/2}$ (dg) and $s_{1/2}d_{3/2}$ (sd) are not distinguished in the CNS formalism. Note that all particles are listed and not just those considered as active (unpaired). Note also that the labels do not refer to the pure j shells, but rather to the dominating amplitudes in the Nilsson orbitals. In some cases, for an odd number of particles in a group, the signature will be specified as a subscript $+(\alpha = +1/2)$ or $-(\alpha = -1/2)$. We will use the so-called Lund convention for the triaxiality parameter γ in relation to the main rotation axis, where for the positive γ shape, $0 < \gamma < 60^\circ$, the rotation (x) axis is the shortest principal axis, while for the negative γ shape, $-60^\circ < \gamma < 0$, it is the intermediate principal axis. In the present calculations for ^{133}La, the $A = 130$ parameters presented in Refs. [7,8] are used.

Energies relative to a standard rotating liquid drop reference, E_{rld} for the experimental bands observed in ^{133}La, are presented in Fig. 6. From this plot, it is possible to distinguish three groups of bands with different behaviors: (i) the low-spin bands, $Q1$–$Q7$, which are all upsloping, (ii) the medium-spin bands, $D1$–$D4$, which have a parabolic behavior with minima at $I = 10$–$15\hbar$, and (iii) the high-spin bands $Q8$, $Q9$, and $Q10$, which exhibit a parabolic behavior with minima at higher spins, $I = 15$–$25\hbar$.

The D bands are recognized in Fig. 6 as nearly degenerate signature doublet sequences. The lack of signature splitting signifies an instability of the tilt of the rotational axis with

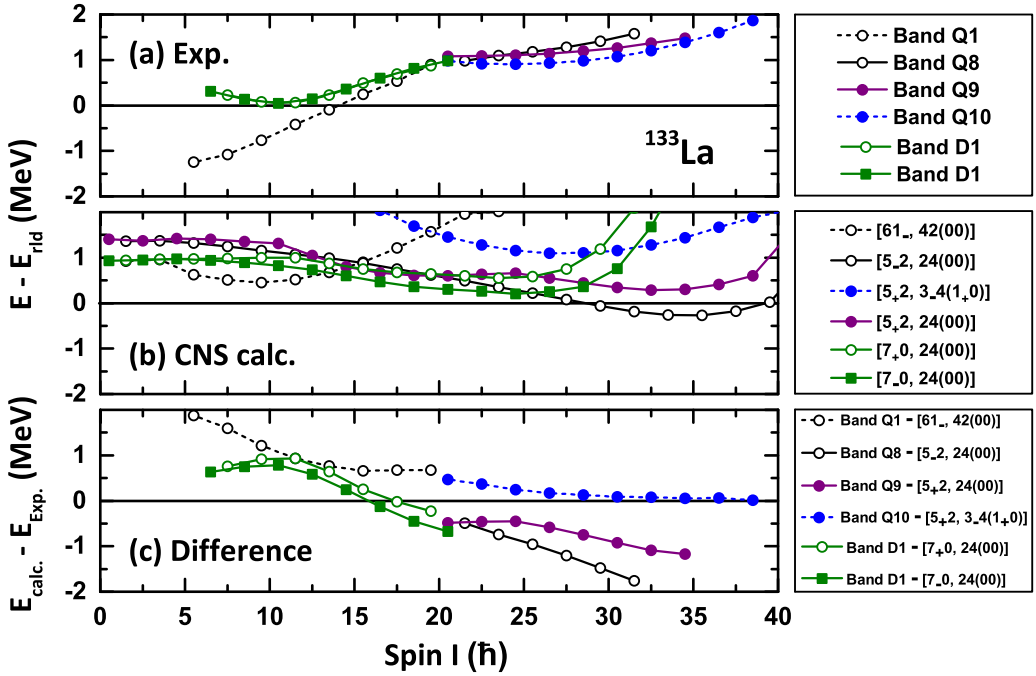

FIG. 7. The observed bands of ^{133}La are presented relative to a rotating liquid drop reference in the upper panel, while the calculated configurations assigned to these bands are given relative to the same reference in the middle panel. The lower panel provides the difference between calculations and experiment.

respect to the principal axes and, hence, the need to carry out tilted axis cranking (TAC) calculations. Nevertheless, the shape and energy are accounted for by the CNS results with good accuracy.

The lowest proton configuration has seven protons in the $\pi(dg)$ positive-parity subshell. Higher angular momenta from proton configurations can be obtained by exciting protons from the $\pi(dg)$ to the $\pi h_{11/2}$ states. The lowest neutron configuration has one hole in the $\nu(sd)$ positive-parity subshell. Higher angular momenta from neutron configurations can be obtained with neutron holes in the $\nu h_{11/2}$ orbital, or with neutron particles in the $\nu(hf)$ and $\nu i_{13/2}$ states above the $N = 82$ spherical shell closure. For strongly deformed configurations, proton excitations from $\pi g_{9/2}$ can also contribute.

As in the case of other triaxial bands observed in this mass region, the variation of the energy relative to a rotating liquid drop has a parabola-like behavior for many medium- and high-spins bands. On the other hand, the lowest excited bands involving only a single proton have an upsloping behavior with increasing spin, which is due to the increasing importance of pairing with decreasing spin as recently discussed, for example, in Ref. [25]. The configuration assignments discussed below are proposed in such a way that the best possible agreement is achieved between experimental and calculated minima and excitation energies.

The comparison between the experimental bands and the CNS configurations are given in Fig. 7. The lowest-lying CNS configurations compatible with band $D1$ is $[61_-,3_\pm3_\pm(00)]$ [or $\pi h^1 \otimes \nu(sd)^{-1}h^{-1}$ in shell-model notation]. However, the experimental fact that the band $D1$ decays strongly towards the bands Q_1–Q_4 which are based on the $\pi(d_{5/2},g_{7/2})$ orbitals, practically excludes this configuration assignment for band $D1$. The next low-lying CNS configurations with three active particles are $[7_\pm0,24(00)]$ [or $\pi(d_{5/2},g_{7/2})^1 \otimes \nu(h_{11/2})^{-2}$ in shell-model notation]. This configuration accounts for the strong decay towards the bands Q_1–Q_4, but does not show the degeneracy observed experimentally (see Fig. 7), which, however, can be induced by the approximation of principal axis rotation adopted in CNS calculations. The calculated deformation of the $[7_\pm0,24(00)]$ configuration assigned to band $D1$ changes smoothly from $(\varepsilon_2,\gamma) \approx (0.16, -25^\circ)$ at $I = 13/2$ to $(\varepsilon_2,\gamma) \approx (0.13, -46^\circ)$ at $I = 39/2$.

For band $D4$, the CNS results are not satisfactory. The calculated CNS configurations $\pi(h_{11/2})^1 \otimes \nu(h_{11/2})^{-2}$ and $\pi(h_{11/2})^3 \otimes \nu(h_{11/2})^{-2}$ assigned to the low- and high-spin parts of this band, based on the analysis of the quasiparticle alignments, are not in agreement with the data. A more elaborate discussion of band $D4$ in the framework of the particle-rotor model (PRM) is provided in the next section.

The proposed CNS configuration of band $Q1$ is $[61_-,42(00)]$ (or $\pi h_{11/2}$ in shell-model notation). Its calculated quadrupole deformation is higher than that of band $D1$ and changes slightly from $\varepsilon_2 \sim 0.19$ at $I = 11/2$ to $\varepsilon_2 \sim 0.17$ at $I = 39/2$, while the triaxiality parameter remains nearly constant ($\gamma \sim +22^\circ$). As can be seen in Fig. 7, the difference between the CNS calculation and the experimental band rises sharply at low spins, indicating the presence of important pairing correlations in this one-particle configuration. The difference between CNS calculations and the data increases at low spins for all assigned configurations, but the extent is less in configurations involving a higher number of active particles, in which the pairing correlations are expected to be quenched.

The configuration assigned to band $Q8$, which continues band $D1$ at higher spins, is [5_2,24(00)] [or $\pi(d_{5/2},g_{7/2})^1(h_{11/2})^2 \otimes \nu(h_{11/2})^{-2}$ in shell-model notation], involving two more protons in $h_{11/2}$ relative to band $D1$. The calculated deformation of the [5_2,24(00)] configuration assigned to band $Q8$ changes smoothly from $(\varepsilon_2,\gamma) \approx (0.16, -40^\circ)$ at $I = 43/2$ to $(\varepsilon_2,\gamma) \approx (0.13,-35^\circ)$ at $I = 63/2$.

Bands $Q9$ and $Q10$ are not linked to low-lying states; therefore their energies, spins, and parities are not known experimentally but only estimated based on the decay pattern. The main difference between bands $Q9$ and $Q10$ is that the latter is observed to higher spins. This suggests a configuration for $Q10$ which involves more high-j particles than that for $Q9$, with possible neutron excitations to the $\nu(hf)$ orbitals above the $N = 82$ spherical shell closure, which will induce a higher deformation. The preferred CNS configuration for $Q9$, taking also into account that its alignment is similar to that of band $Q8$ (see Fig. 5), is [5+2,24(00)], which similar to that of band $Q8$ but involves the opposite signature of the $\pi(dg)$ orbital. The lowest-lying CNS configuration compatible with band $Q10$ is [5+2,3_4(1+0)], which involves one more neutron excited to the $\nu(hf)$ orbital relative to band $Q9$. The calculated deformation of the [5+2,24(00)] configuration proposed for band $Q9$ varies smoothly from $(\varepsilon_2,\gamma) \approx (0.17, -41^\circ)$ at $I = 45/2$ to $(\varepsilon_2,\gamma) \approx (0.11, -35^\circ)$ at $I = 69/2$. The calculated deformation of the [5+2,3_4(1+0)] configuration assigned to band $Q10$ is larger and changes smoothly from $(\varepsilon_2,\gamma) \approx (0.21,+25^\circ)$ at $I = 41/2$ to $(\varepsilon_2,\gamma) \approx (0.15, +29^\circ)$ at $I = 77/2$.

One should note the positive γ values for the configurations assigned to the bands $Q1$ and $Q10$, which are opposite to those calculated for the configurations assigned to bands $Q8$ and $Q9$, indicating rotations around different axes of the triaxial ellipsoid—the short axis for $Q1$, $Q10$ and the intermediate axis for $Q8$, $Q9$—as recently reported for similar high-spin bands in ^{138}Nd [26].

C. CDFT calculations with self-consistent RMF

The configurations assigned from the quasiparticle alignment analysis and the CNS calculations were investigated further using constrained triaxial covariant density functional theory calculations [11] including (i) the potential-energy surface (PES) in the (β_2,γ) plane of Fig. 8 and (ii) the potential energy surface as a function of β_2 (minimized with γ) of Fig. 9. It should be noted that the quadrupole deformation parameter ε_2 used in CNS calculations differs slightly from the β_2 one used in CDFT and PRM calculations. However, as the difference between ε_2 and β_2 is small, it has been neglected in the following discussion.

1. Potential energy surfaces in the (β_2,γ) plane

Self-consistent, constrained calculations in the two-dimensional (β_2, γ) plane are essential not only to investigate the γ stiffness for the ^{133}La nucleus, but also to check consistency with the deformation parameters calculated by the CNS model. The PES of the ground-state configuration obtained by the constrained triaxial CDFT calculations with the effective interaction PC-PK1 [27] is presented in Fig. 8. In

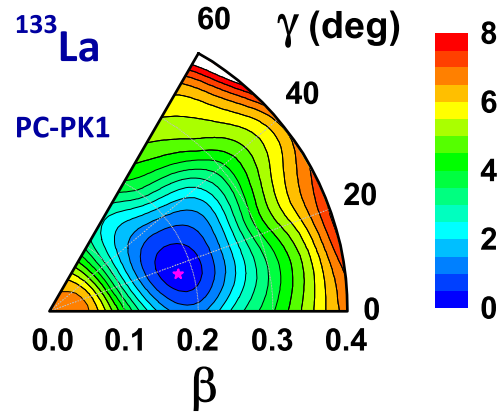

FIG. 8. Potential-energy surface in the β_2-γ plane ($0 \leqslant \beta_2 \leqslant 0.4, 0 \leqslant \gamma \leqslant 60^\circ$) for the ground-state configuration of ^{133}La in constrained triaxial RMF calculations with the PC-PK1 effective interaction. All energies are normalized with respect to the energy of the absolute minimum (in MeV) indicated by the star. The energy separation between each contour line is 0.5 MeV.

the constrained CDFT calculations, the Dirac equation for the nucleons is solved in a three-dimensional harmonic oscillator basis, which in the present case includes 12 major oscillator shells. The pairing correlations are neglected. The PES is obtained by constraining the (β_2,γ) deformation parameters to vary in the intervals $\beta_2 \in [0.0,0.4]$ and $\gamma \in [0^\circ,60^\circ]$, with step sizes $\Delta\beta = 0.05$ and $\Delta\gamma = 6^\circ$, respectively. The energies are normalized with respect to the binding energy of the absolute minimum (labeled with a star symbol in Fig. 8). It is found that the ground state of ^{133}La has a deformation $(\beta_2,\gamma) = (0.19,16^\circ)$ and a moderate γ softness. The CDFT and CNS deformation parameters are in good overall agreement.

2. Potential-energy curve as function of the β_2 deformation

By minimizing the energy with respect to the γ deformation, both adiabatic and configuration-fixed constrained

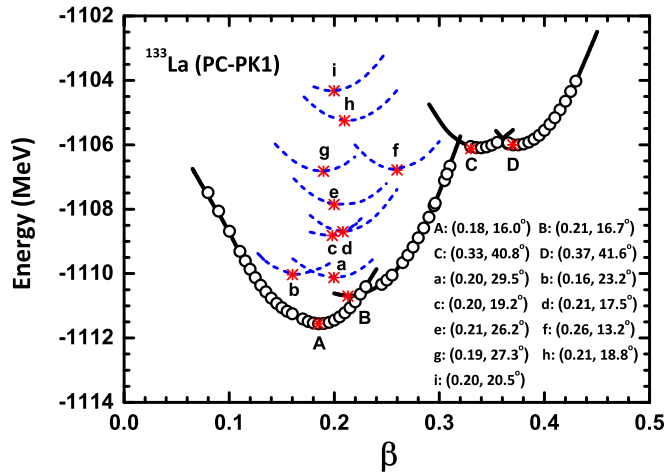

FIG. 9. The potential energy as a function of β_2 in adiabatic (open circles) and configuration-fixed (lines) constrained triaxial RMF calculations with the PC-PK1 effective interaction for ^{133}La.

TABLE II. The excitation energies E_x, deformation parameters β_2 and γ, configurations (valence nucleons and active nucleons), and the parities of minima for states A–D and a–e in the configuration-fixed constrained triaxial RMF calculations. The observed band associated with each state is given in the last column.

State	E_x(MeV)	(β_2,γ)	Valence nucleon configuration	Active nucleon configuration	π	Band
A	0.00	(0.18,16.0°)	$\pi d_{5/2}^2 g_{7/2}^{-3} \otimes \nu(s_{1/2},d_{3/2})^{-2} h_{11/2}^{-4}$	$\pi g_{7/2}^{-1}$	+	$Q4$
B	0.85	(0.21,16.7°)	$\pi d_{5/2}^2 g_{7/2}^{-4} h_{11/2}^1 \otimes \nu(s_{1/2},d_{3/2})^{-2} h_{11/2}^{-4}$	$\pi h_{11/2}^1$	−	$Q1$, $Q2$
C	5.44	(0.33,40.8°)	$\pi d_{5/2}^2 g_{7/2}^{-4} h_{11/2}^2 p_{3/2}^{-1} \otimes \nu(g_{7/2},d_{5/2})^{-6} h_{9/2}^2 h_{11/2}^{-2}$	$\pi p_{3/2}^{-1} \otimes \nu h_{9/2}^2$	−	
D	5.55	(0.37,41.6°)	$\pi d_{3/2}^2 g_{7/2}^{-4} h_{11/2}^3 p_{3/2}^{-2} \otimes \nu(g_{7/2},d_{5/2})^{-6} h_{9/2}^2 h_{11/2}^{-2}$	$\pi h_{11/2}^1 \otimes \nu h_{9/2}^2$	−	
a	1.43	(0.20,29.5°)	$\pi d_{5/2}^2 g_{7/2}^{-4} h_{11/2}^1 \otimes \nu(s_{1/2},d_{3/2})^{-3} h_{11/2}^{-3}$	$\pi h_{11/2}^1 \otimes \nu(s_{1/2},d_{3/2})^{-1} h_{11/2}^{-1}$	+	
b	1.52	(0.16,23.2°)	$\pi d_{5/2}^1 g_{7/2}^{-2} \otimes \nu(s_{1/2},d_{3/2})^{-2} h_{11/2}^{-4}$	$\pi d_{5/2}^1 \otimes \nu h_{11/2}^{-2}$	+	$D1$, $D2$
c	2.74	(0.20,19.2°)	$\pi d_{5/2}^2 g_{7/2}^{-4} h_{11/2}^1 \otimes \nu(s_{1/2},d_{3/2})^{-2} h_{11/2}^{-4}$	$\pi h_{11/2}^1 \otimes \nu h_{11/2}^{-2}$	−	$D4$-low
d	2.86	(0.21,17.4°)	$\pi d_{5/2}^1 g_{7/2}^{-4} h_{11/2}^2 \otimes \nu(s_{1/2},d_{3/2})^{-2} h_{11/2}^{-4}$	$\pi d_{5/2}^1 h_{11/2}^2 \otimes \nu h_{11/2}^{-2}$	+	
e	3.70	(0.21,26.2°)	$\pi d_{5/2}^1 g_{7/2}^{-4} h_{11/2}^2 \otimes \nu(s_{1/2},d_{3/2})^{-3} h_{11/2}^{-3}$	$\pi d_{5/2}^1 h_{11/2}^2 \otimes \nu(s_{1/2},d_{3/2})^{-1} h_{11/2}^{-1}$	−	
f	4.67	(0.26,13.2°)	$\pi d_{5/2}^1 g_{7/2}^{-4} h_{11/2}^2 \otimes \nu(s_{1/2},d_{3/2})^{-3} h_{11/2}^{-4} (f_{7/2},h_{9/2})^1$	$\pi d_{5/2}^1 h_{11/2}^2 \otimes \nu(s_{1/2},d_{3/2})^{-1} h_{11/2}^{-2} (f_{7/2},h_{9/2})^1$	−	$Q10$
g	4.71	(0.19,27.3°)	$\pi d_{5/2}^1 g_{7/2}^{-4} h_{11/2}^2 \otimes \nu(s_{1/2},d_{3/2})^{-2} h_{11/2}^{-4}$	$\pi d_{5/2}^1 h_{11/2}^2 \otimes \nu h_{11/2}^{-2}$	+	$Q8$, $Q9$
h	6.30	(0.21,18.8°)	$\pi g_{7/2}^{-4} h_{11/2}^3 \otimes \nu(s_{1/2},d_{3/2})^{-3} h_{11/2}^{-3}$	$\pi h_{11/2}^3 \otimes \nu(s_{1/2},d_{3/2})^{-1} h_{11/2}^{-1}$	+	
i	7.23	(0.20,20.5°)	$\pi g_{7/2}^{-4} h_{11/2}^3 \otimes \nu(s_{1/2},d_{3/2})^{-2} h_{11/2}^{-4}$	$\pi h_{11/2}^3 \otimes \nu h_{11/2}^{-2}$	−	$D4$-high

triaxial RMF calculations [6,11,28–30] have been performed for the possible configurations associated with the observed bands in ^{133}La. In the constrained RMF calculations, no rotation is considered. This is because the constrained CDFT calculations were performed without rotation. The results of the configuration-fixed constrained calculations for the possible configurations of the dipole bands [Figs. 9(a)–9(c) and 9(i)] and of the bands $Q8$, $Q9$, and $Q10$ [Figs. 9(d)–9(h)] are shown. The excitation energy E_x, deformation parameters, the valence and active nucleons, and the parity of the configurations corresponding to these minima are summarized in Table II. One can identify several regions in the adiabatic configurations (open circles in Fig. 9), which correspond to different configurations. The curves drawn with continuous lines correspond to constrained calculations for fixed configurations, which have the local minima A, B, C, and D. It is found that all these minima correspond to configurations with one active proton and zero or two active neutrons (see the fifth column of Table II).

3. *Configuration information*

The configuration with the minimum A in Fig. 9 corresponds to the ground-state band $Q4$, with a triaxial deformation $(\beta_2,\gamma) = (0.18,16°)$. The valence nucleon configuration is $\pi d_{5/2}^2 g_{7/2}^{-3} \otimes \nu(s_{1/2},d_{3/2})^{-2} h_{11/2}^{-4}$. Since two $\pi d_{5/2}$ proton particles, two $\pi g_{7/2}$ proton holes, and six $\nu(s_{1/2},d_{3/2})$ and $\nu h_{11/2}$ neutron holes are paired and have no contribution to the total angular momentum, the unpaired nucleon configuration is $\pi g_{7/2}^{-1}$. The configurations associated with the minima B, C, and D all have negative parity. The configurations with the minima B and D have the same unpaired proton configuration $\pi h_{11/2}^1$, but a different neutron configuration and deformation parameters. Considering that the configuration with minimum B is energetically favored, it is natural to assign it to bands $Q1$ and $Q2$. The quadrupole deformation parameter of configuration B is similar in CDFT and CNS calculations (i.e., $\beta_2 \sim 0.21$), while the triaxial deformation is slightly lower in the CDFT calculations ($\gamma = 16.7°$) than in the CNS ones ($\gamma = 22°$).

We calculated three configurations involving three active quasiparticles (a, b, and c), five involving five quasiparticles (d, e, g, h, and i), and one involving seven quasiparticles (f). The configurations c, e, and f have negative parity, while the remaining ones have positive parity. The triaxial deformation parameter of the configuration b assigned to bands $D1$ and $D2$ is 23.2°, lower by ∼2° than that derived from CNS calculations. The configurations c and i have very similar deformation parameters and are assigned to the low- and high-spin parts of band $D4$, respectively (see the discussion in Sec. IV A). The deformations of the c–h configurations differ from those of the CNS calculations, having larger β_2 and smaller γ values.

D. PRM calculations

With the configurations and deformation parameters obtained from the constrained CDFT calculations, it is straightforward to perform PRM calculations [6,12–15] in order to study the energy spectra and the electromagnetic transition probabilities for the observed sequences in ^{133}La.

In the PRM calculations, with input deformation parameters β_2 and γ taken from the aforementioned CDFT calculations, the single-j shell Hamiltonian parameter [31] is taken as

$$C = \left(\frac{123}{8}\sqrt{\frac{5}{\pi}}\right)\frac{2N+3}{j(j+1)}A^{-1/3}\beta_2, \qquad (1)$$

where N denotes the number of oscillator quanta. For the electromagnetic transitions, the empirical intrinsic quadrupole moment $Q_0 = (3/\sqrt{5\pi})R_0^2 Z\beta_2$ with $R_0 = 1.2A^{1/3}$fm, gyromagnetic ratio $g_R = 0.43$, $g_\pi(g_{9/2}) = 1.26$, $g_\pi(h_{11/2}) =$

1.21, $g_\pi(2d_{5/2}) = 1.47$, and $g_\nu(h_{11/2}) = -0.21$, and are adopted [13].

1. Bands D1, D2, and Q8, Q9

The configurations assigned to bands $D1$ and $D2$ are $\pi d^1_{5/2} \otimes \nu h^{-2}_{11/2}$ (see Sec. IV A). The input deformation parameters are taken from the configuration-fixed constrained triaxial CDFT calculations, which are $(\beta_2,\gamma) = (0.16,23.2^\circ)$ (see Table II). For the bands $Q8$ and $Q9$ the assigned configuration is $\pi d^1_{5/2} h^2_{11/2} \otimes \nu h^{-2}_{11/2}$ with CDFT deformation parameters $(\beta_2,\gamma) = (0.19,27.3^\circ)$. The moments of inertia are adjusted to reproduce the trend of the energy spectra of the different bands; the adopted values are $\mathcal{J}_0 = 19\hbar^2/\text{MeV}$ for bands $D1$ and $D2$, and $\mathcal{J}_0 = 41\hbar^2/\text{MeV}$ for bands $Q8$ and $Q9$. It is noted that the moments of inertia used in the two calculations differ quite a bit. This can be understood by the fact that the bands $Q8$ and $Q9$ involve one additional $h_{11/2}$ proton pair, which can contribute a larger alignment (see Fig. 5), as well as larger moments of inertia compared with the bands $D1$ and $D2$. A Coriolis attenuation factor $\xi = 0.96$ is employed to describe the data for the bands $D1$ and $D2$, while a factor $\xi = 0.90$ is employed to describe the data for the bands $Q8$ and $Q9$ [6].

The calculated energy spectra and the $B(M1)/B(E2)$ branching ratios are compared with the data in Fig. 10, where the PRM results are seen to be in good agreement with the data. The energy separation of the doublet bands $D1$ and $D2$ varies from $\sim$100 keV at $I = 19/2\hbar$ to $\sim$200 keV at $I = 29/2\hbar$. The energy difference between the doublet bands is small since their triaxial deformation is close to $\gamma = 30^\circ$, best suited for the chiral doublet degeneracy [32]. The calculated $B(M1)/B(E2)$ values of bands $D1$ and $D2$ have a similar behavior, reproducing the decreasing trend with increasing spin observed experimentally, but also showing a pronounced discrepancy at low spins.

Band $Q8$ is the continuation at higher spins of the negative-signature partner of band $D1$. The PRM calculations can reproduce its experimental energy spectrum rather well, herewith confirming the assigned five-quasiparticle configuration involving two additional $\pi h_{11/2}$ protons relative to band $D1$. It should be noted that, in the PRM calculations, due to the assumption of a frozen core, the bandhead energy has to be chosen by hand to reproduce the overall trend of the data. Therefore, the extent of competition between the three- and five-quasiparticle configurations cannot be estimated directly from the data.

From the eigenfunctions calculated by PRM, one can derive the angular momentum geometry of a given configuration [12]. In Fig. 11, the expectation values of the squared angular momentum components of the core, $R_k = \sqrt{\langle \hat{R}^2_k \rangle}$, of the active neutron, $J_{\nu k} = \sqrt{\langle \hat{J}^2_{\nu k} \rangle}$, and of the active proton, $J_{\pi k} = \sqrt{\langle \hat{J}^2_{\pi k} \rangle}$, are presented for bands $D1$, $D2$ and $Q8$, $Q9$. As can be seen, the angular momentum of the collective core for both bands $D1$ and $D2$ is mainly aligned along the intermediate axis (i axis), which corresponds to the largest moment of inertia. The angular momentum of the $\pi d_{5/2}$ active proton particle is mainly aligned along the short axis (s axis), while that of the $\nu h_{11/2}$ neutron holes is aligned mainly along the long axis (l axis) at low spins and gradually aligns along a $3D$ direction at high spins. This is compatible with a chiral rotation, even though the spin carried by the $\pi d_{5/2}$ proton particle is much smaller than the spin of the two $\nu h_{11/2}$ active neutron holes. The $3D$ chiral geometry is realized because the angular momentum components of the two $\nu h_{11/2}$ neutron holes present in the configurations of bands $D1$, $D2$ are significant not only along the l axis, but also along the s axis, compensating for the smaller spin of the $\pi d_{5/2}$ active proton mainly aligned along the s axis. Thus, the $3D$ chiral geometry, which requires significant angular momentum projections along all three axes of the intrinsic reference system, exists in bands $D1$ and $D2$.

For the bands $Q8$ and $Q9$, the projection of the angular momentum on the three axes exhibits a discontinuous jump relative to those of the bands $D1$ and $D2$, which marks the change from the three-quasiparticle configuration of bands $D1$

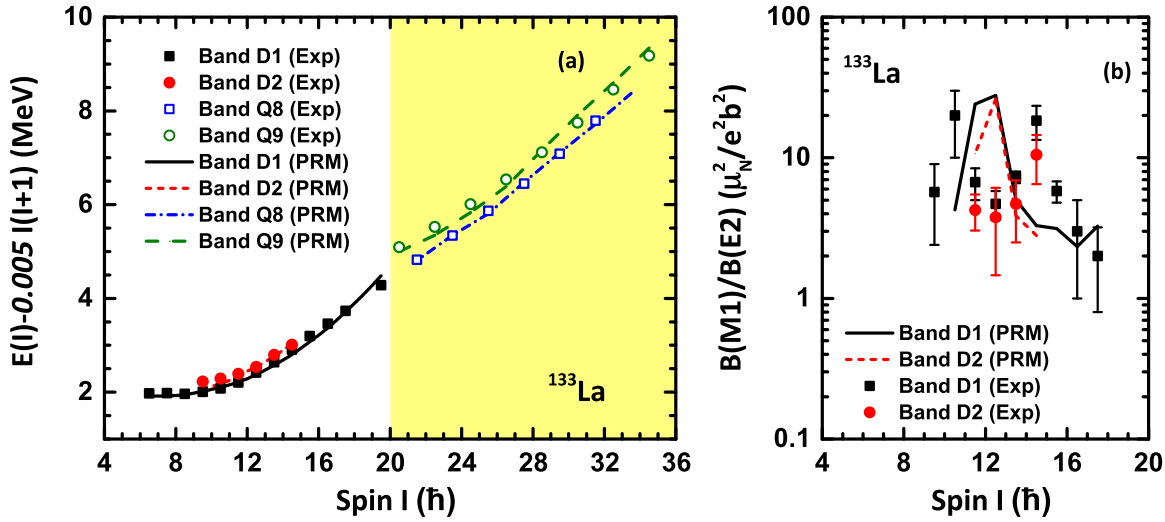

FIG. 10. The results of PRM calculations in comparison with experimental data: (a) the energies $E(I)$, less than a reference ε, for bands $D1$, $D2$ and $Q8$, $Q9$ for the configurations assigned in the present work; (b) the $B(M1)/B(E2)$ ratios for bands $D1$ and $D2$ for the proposed configurations.

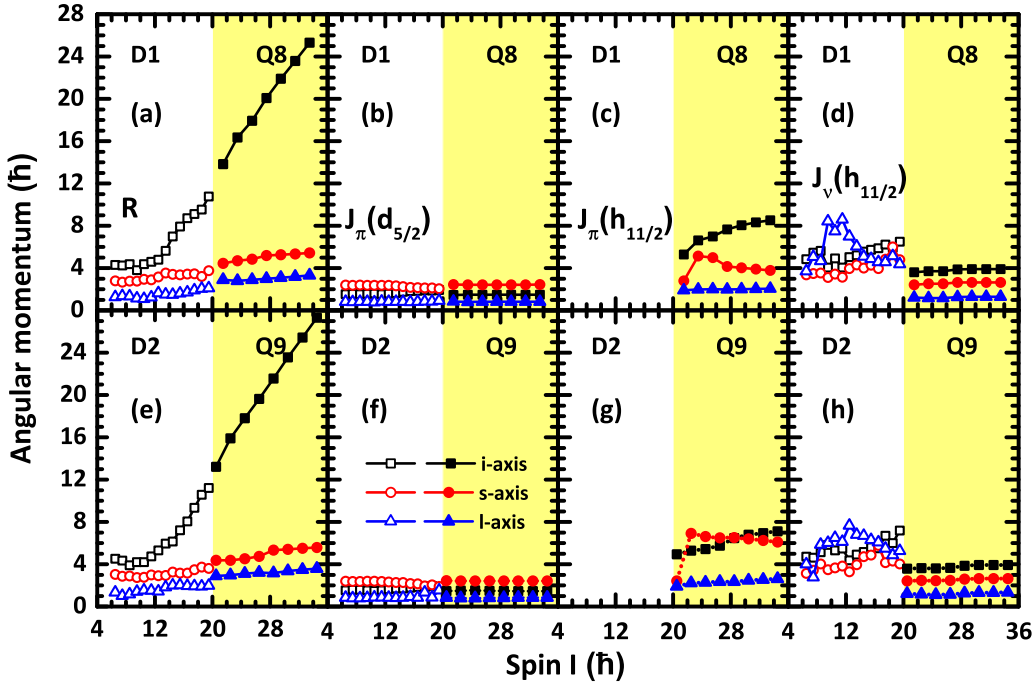

FIG. 11. The root mean square components along the intermediate (i, squares), short (s, circles), and long (l, triangles) axes of the core $R_k = \sqrt{\langle \hat{R}_k^2 \rangle}$, the active neutron $J_{nk} = \sqrt{\langle \hat{j}_{nk}^2 \rangle}$, and the active proton $J_{pk} = \sqrt{\langle \hat{j}_{pk}^2 \rangle}$ calculated as a function of spin by means of the PRM for bands $D1$, $D2$, and $Q8$, $Q9$ in ^{133}La.

and $D2$ to a five-quasiparticle one, involving two additional $\pi h_{11/2}$ protons. The angular momentum of the core is mainly aligned along the i axis. This component increases linearly with increasing spin. The three proton particles present in the configuration of bands $Q8$ and $Q9$ have their angular momenta aligned along the i axis as well, with higher component along the s axis for $Q9$. Compared to bands $D1$ and $D2$, the two $\pi h_{11/2}$ protons have the angular momentum tilted in the i-s plane away from the s axis. The angular momenta of the $\nu h_{11/2}$ neutron holes are aligned along the i axis as well. Consequently, the total angular momentum of the nucleus in band $Q8$ is mainly aligned along the i axis, inducing a principal axis rotation and a corresponding band consisting of $E2$ transitions, as observed experimentally. This is a case where a transition occurs from an aplanar rotation to a principal axis one in going from the bands $D1$, $D2$ to $Q8$, $Q9$, induced by the change from a three- to a five-quasiparticle excitation.

2. *Band D4*

As discussed in Sec. IV A, the possible configuration of the low-spin part of band $D4$ ($I \leqslant 37/2\hbar$) is proposed to be the three-quasiparticle configuration $\pi h_{11/2}^{1} \otimes \nu h_{11/2}^{-2}$, while that of the high-spin part ($I \geqslant 39/2\hbar$) is the $\pi h_{11/2}^{3} \otimes \nu h_{11/2}^{-2}$ five-quasiparticle one. The CDFT deformation parameters of these configurations are $(\beta_2,\gamma) = (0.20, 19.2^\circ)$ and $(0.20, 20.5^\circ)$, respectively. As in the calculations of the configuration assigned to bands $D1$, $D2$, and $Q8$, we adopt moments of inertia which reproduce the experimental energy spectrum: For the three- and five-quasiparticle configurations assigned to band $D4$, these are $\mathcal{J}_0 = 25\hbar^2/\text{MeV}$ and $\mathcal{J}_0 = 20\hbar^2/\text{MeV}$, respectively.

The PRM energy spectrum calculated for the configurations assigned to the low- and high-spin parts of band $D4$ are compared with experimental data in Fig. 12: The PRM results are in good agreement with the experimental data. For the low-spin, three-quasiparticle configuration, the calculated energies vary smoothly with increasing spin, while for the high-spin, five-quasiparticle one, a pronounced odd-even staggering is calculated, indicative of a significant splitting between the signature partners. Such a splitting could not be

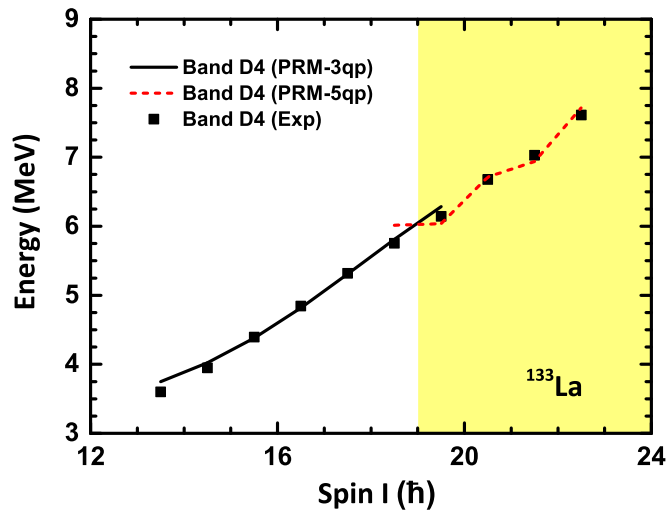

FIG. 12. The energies $E(I)$ for band $D4$ calculated by the PRM (solid and dashed lines) in comparison with the experimental data (solid squares).

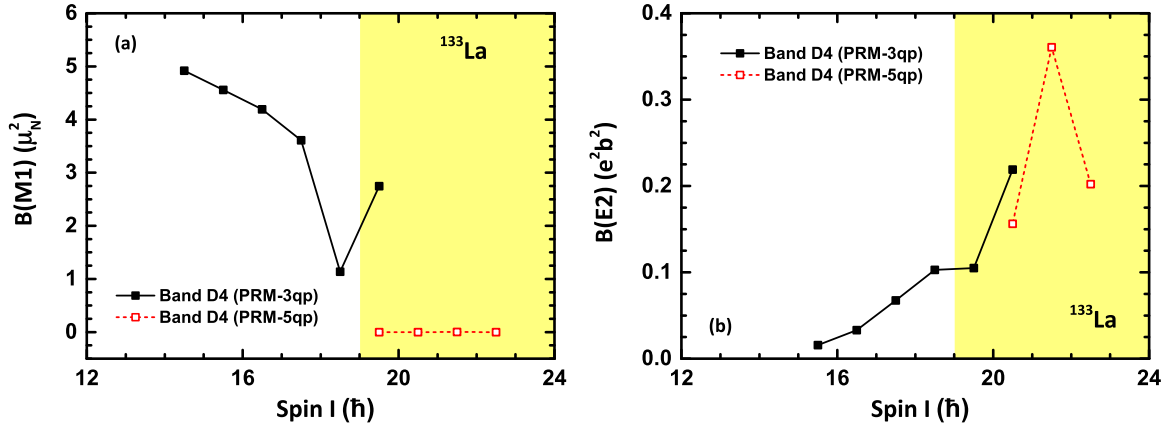

FIG. 13. The reduced transition probabilities $B(M1)$ and $B(E2)$ of band D4 calculated with the PRM.

obtained for the high-spin part of band $D4$ assuming a three-quasiparticle configuration, herewith strongly supporting the five-quasiparticle assignment.

In Fig. 13, the calculated reduced transition probabilities $B(M1)$ and $B(E2)$ for the configurations assigned to the low- and high-spin parts of band $D4$ are shown as a function of spin. Experimentally, only the 923-keV crossover transition is observed. So, no experimental $B(M1)/B(E2)$ values are available, except that for the $35/2^-$ level which is $5.4(6)\mu_N^2/e^2b^2$. The calculated $B(M1)/B(E2)$ branching ratio is $\sim 50\mu_N^2/e^2b^2$. For the low-spin part of band $D4$ ($I \leqslant 18.5\hbar$), the $B(M1)$ values decrease with spin, while the $B(E2)$ ones increase, suggesting that the collective behavior becomes gradually more important. The calculated $B(M1)$ value for the $I = 39/2\hbar$ state of the three-quasiparticle configuration shows a sudden increase, which can be understood by analyzing the angular momentum geometry (see below). In the high-spin part of band $D4$ ($I \geqslant 39/2\hbar$), due to the appearance of signature splitting, the $B(M1)$ values vanish and the $B(E2)$ rates exhibit an odd-even staggering. Since, in the low-spin part, the $B(M1)$ values are large (a few μ_N^2) and the $B(E2)$ rates are small ($<0.1e^2b^2$), band $D4$ can be interpreted as a magnetic rotation band [33]. Lifetime measurements are imperative to reach a definitive conclusion on the possible magnetic rotation character of this band.

To investigate the angular momentum geometry of band $D4$, the expectation values of the squared angular momentum components of the core, of the active protons, and of the active neutrons are indicated in Fig. 14. For the low-spin part, as expected, the angular momenta of the core, of the active proton particle, and of the active neutron holes are mainly aligned along the i, s, and l axes, respectively. It should be noted that, for the core, the projection on the s axis is not negligible, driving the angular momentum of the core into the s-i plane. The angular momenta of the two $\nu h_{11/2}$ neutron holes have rather large components along the l axis. Consequently, the total angular momentum of band $D4$ is aplanar but close to the l-s plane. This can explain why the experimentally observed band has the characteristics of a $\Delta I = 1$ band. At $I = 37/2\hbar$, an important jump occurs in the calculated angular momentum along the s and i axes, which corresponds to a sizable increase of the $B(M1)$ value. In the high-spin region, the angular momenta display an obvious odd-even staggering, especially for the neutron holes. This is correlated with the signature splitting of the calculated energies. It is interesting to note that, after the breaking of one proton pair, the behavior of the neutron angular momentum along the l axis also changes rather dramatically. The reasons behind this correlation are not yet understood.

V. SUMMARY

The level structure of ^{133}La has been investigated using the ^{116}Cd(^{22}Ne , $p4n$) reaction in high-statistics Gammasphere experiments. Four new bands have been identified, and the previously reported level scheme is revised and extended to higher spins. Detailed calculations using three formalisms (CNS, CDFT, and PRM) have been performed to understand the structure of the observed bands, which are based on triaxial configurations. For the high-spin bands it is found that rotations around different axes can occur, depending on the configuration. The orientation of the angular momenta of the core and of the active particles is investigated, revealing chiral rotation for two nearly degenerate dipole bands and magnetic character for one dipole band. It is shown that the $h_{11/2}$ neutron holes present in the configuration of the nearly

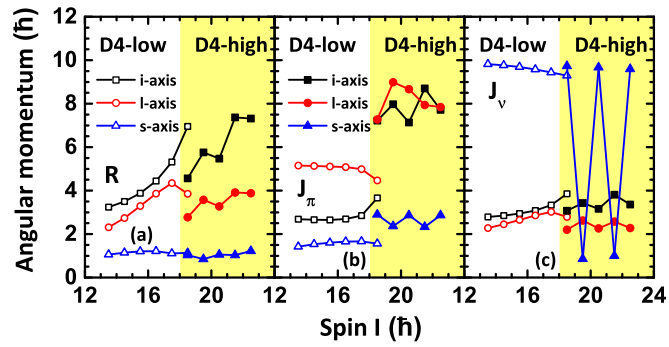

FIG. 14. The root mean square components along the intermediate (i, squares), short (s, circles), and long (l, triangles) axis of the core $R_k = \sqrt{\langle \hat{R}_k^2 \rangle}$, the active neutron $J_{nk} = \sqrt{\langle \hat{J}_{nk}^2 \rangle}$, and the active proton $J_{pk} = \sqrt{\langle \hat{J}_{pk}^2 \rangle}$ calculated as a function of spin by means of the PRM for band $D4$.

degenerate dipole bands have significant angular momentum components not only along the long axis but also along the short axis, contributing to the balance of the angular momentum components along the short and long axes and thus giving rise to a chiral geometry.

ACKNOWLEDGMENTS

This work has been supported in part by the U.S. National Science Foundation (Grants No. PHY07-58100, No. PHY-1068192, and No. PHY-1419765), the U.S. Department of Energy, Office of Science, Office of Nuclear Physics, under Grant No. DE-FG02-94ER40834 (U.M.) and Contract No. DE-AC02-06CH11357 (A.N.L.), the Chinese Major State 973 Program No. 2013CB834400, the National Natural Science Foundation of China (Grants No. 11175002, No. 11335002, No. 11375015, and No. 11461141002), the Research Fund for the Doctoral Program of Higher Education (Grant No. 20110001110087), and the China Postdoctoral Science Foundation under Grants No. 2015M580007 and No. 2016T90007. This research used resources of ANL's ATLAS facility, which is a DOE Office of Science User Facility.

[1] J. T. Matta, U. Garg, W. Li, S. Frauendorf, A. D. Ayangeakaa, D. Patel, K. W. Schlax, R. Palit, S. Saha, J. Sethi, T. Trivedi, S. S. Ghugre, R. Raut, A. K. Sinha, R. V. F. Janssens, S. Zhu, M. P. Carpenter, T. Lauritsen, D. Seweryniak, C. J. Chiara, F. G. Kondev, D. J. Hartley, C. M. Petrache, S. Mukhopadhyay, D. V. Lakshmi, M. K. Raju, P. V. Madhusudhana Rao, S. K. Tandel, S. Ray, and F. Dönau, Phys. Rev. Lett. **114**, 082501 (2015).
[2] S. Frauendorf and J. Meng, Nucl. Phys. A **617**, 131 (1997).
[3] T. Koike, K. Starosta, C. J. Chiara, D. B. Fossan, and D. R. LaFosse, Phys. Rev. C **63**, 061304 (2001).
[4] K. Starosta, T. Koike, C. J. Chiara, D. B. Fossan, D. R. LaFosse, A. A. Hecht, C. W. Beausang, M. A. Caprio, J. R. Cooper, R. Krücken, J. R. Novak, N. V. Zamfir, K. E. Zyromski, D. J. Hartley, D. L. Balabanski, J.-Y. Zhang, S. Frauendorf, and V. I. Dimitrov, Phys. Rev. Lett. **86**, 971 (2001).
[5] R. Bark, A. Baxter, A. Byrne, G. Dracoulis, T. Kibédi, T. McGoram, and S. Mullins, Nucl. Phys. A **691**, 577 (2001).
[6] A. D. Ayangeakaa, U. Garg, M. D. Anthony, S. Frauendorf, J. T. Matta, B. K. Nayak, D. Patel, Q. B. Chen, S. Q. Zhang, P. W. Zhao, B. Qi, J. Meng, R. V. F. Janssens, M. P. Carpenter, C. J. Chiara, F. G. Kondev, T. Lauritsen, D. Seweryniak, S. Zhu, S. S. Ghugre, and R. Palit, Phys. Rev. Lett. **110**, 172504 (2013).
[7] A. Afanasjev, D. Fossan, G. Lane, and I. Ragnarsson, Phys. Rep. **322**, 1 (1999).
[8] T. Bengtsson and I. Ragnarsson, Nucl. Phys. A **436**, 14 (1985).
[9] B. G. Carlsson and I. Ragnarsson, Phys. Rev. C **74**, 011302 (2006).
[10] A. Afanasjev and I. Ragnarsson, Nucl. Phys. A **591**, 387 (1995).
[11] J. Meng, J. Peng, S. Q. Zhang, and S.-G. Zhou, Phys. Rev. C **73**, 037303 (2006).
[12] B. Qi, S. Zhang, J. Meng, S. Wang, and S. Frauendorf, Phys. Lett. B **675**, 175 (2009).
[13] B. Qi, S. Q. Zhang, S. Y. Wang, J. Meng, and T. Koike, Phys. Rev. C **83**, 034303 (2011).
[14] E. O. Lieder, R. M. Lieder, R. A. Bark, Q. B. Chen, S. Q. Zhang, J. Meng, E. A. Lawrie, J. J. Lawrie, S. P. Bvumbi, N. Y. Kheswa, S. S. Ntshangase, T. E. Madiba, P. L. Masiteng, S. M. Mullins, S. Murray, P. Papka, D. G. Roux, O. Shirinda, Z. H. Zhang, P. W. Zhao, Z. P. Li, J. Peng, B. Qi, S. Y. Wang, Z. G. Xiao, and C. Xu, Phys. Rev. Lett. **112**, 202502 (2014).
[15] I. Kuti, Q. B. Chen, J. Timár, D. Sohler, S. Q. Zhang, Z. H. Zhang, P. W. Zhao, J. Meng, K. Starosta, T. Koike, E. S. Paul, D. B. Fossan, and C. Vaman, Phys. Rev. Lett. **113**, 032501 (2014).
[16] A. D. Ayangeakaa, U. Garg, C. M. Petrache, S. Guo, P. W. Zhao, J. T. Matta, B. K. Nayak, D. Patel, R. V. F. Janssens, M. P. Carpenter, C. J. Chiara, F. G. Kondev, T. Lauritsen, D. Seweryniak, S. Zhu, S. S. Ghugre, and R. Palit, Phys. Rev. C **93**, 054317 (2016).
[17] I.-Y. Lee, Nucl. Phys. A **520**, c641 (1990).
[18] D. Radford, Nucl. Instrum. Meth. Phys. Res. A **361**, 297 (1995).
[19] D. Radford, Nucl. Instrum. Meth. Phys. Res. A **361**, 306 (1995).
[20] V. Iacob and G. Duchene, Nucl. Instrum. Meth. Phys. Res. A **399**, 57 (1997).
[21] A. Krämer-Flecken, T. Morek, R. M. Lieder, W. Gast, G. Hebbinghaus, H. M. Jäger, and W. Urban, Nucl. Instrum. Meth. Phys. Res. A **275**, 333 (1989).
[22] C. J. Chiara, M. Devlin, E. Ideguchi, D. R. LaFosse, F. Lerma, W. Reviol, S. K. Ryu, D. G. Sarantites, O. L. Pechenaya, C. Baktash, A. Galindo-Uribarri, M. P. Carpenter, R. V. F. Janssens, T. Lauritsen, C. J. Lister, P. Reiter, D. Seweryniak, P. Fallon, A. Görgen, A. O. Macchiavelli, D. Rudolph, G. Stoitcheva, and W. E. Ormand, Phys. Rev. C **75**, 054305 (2007).
[23] L. Hildingson, W. Klamra, T. Lindblad, C. G. Lindén, G. Sletten, and G. Székely, Z. Phys. A **338**, 125 (1991).
[24] R. Bengtsson and S. Frauendorf, Nucl. Phys. A **327**, 139 (1979).
[25] C. M. Petrache, I. Ragnarsson, H.-L. Ma, R. Leguillon, T. Zerrouki, D. Bazzacco, and S. Lunardi, Phys. Rev. C **91**, 024302 (2015).
[26] C. M. Petrache, I. Ragnarsson, H.-L. Ma, R. Leguillon, T. Konstantinopoulos, T. Zerrouki, D. Bazzacco, and S. Lunardi, Phys. Rev. C **88**, 051303 (2013).
[27] P. W. Zhao, Z. P. Li, J. M. Yao, and J. Meng, Phys. Rev. C **82**, 054319 (2010).
[28] J. Peng, H. Sagawa, S. Q. Zhang, J. M. Yao, Y. Zhang, and J. Meng, Phys. Rev. C **77**, 024309 (2008).
[29] J. M. Yao, B. Qi, S. Q. Zhang, J. Peng, S. Y. Wang, and J. Meng, Phys. Rev. C **79**, 067302 (2009).
[30] J. Li, S. Q. Zhang, and J. Meng, Phys. Rev. C **83**, 037301 (2011).
[31] W. Shou-Yu, Q. Bin, and Z. Shuang-Quan, Chin. Phys. Lett. **26**, 052102 (2009).
[32] B. Qi, S. Q. Zhang, S. Y. Wang, J. M. Yao, and J. Meng, Phys. Rev. C **79**, 041302 (2009).
[33] J. Meng, J. Peng, S. Q. Zhang, and P. W. Zhao, Front. Phys. **8**, 55 (2013).